ANNUAL REVIEWS

Annual Review of Condensed Matter Physics

Weyl Metals

A.A. Burkov

Department of Physics and Astronomy, University of Waterloo, Waterloo, Ontario N2L 3G1, Canada; email: aburkov@uwaterloo.ca

Keywords

Weyl semimetal, Dirac semimetal, topological insulator, chiral anomaly

Abstract

Weyl metal is the first example of a conducting material with a nontrivial electronic structure topology, making it distinct from an ordinary metal. Unlike in insulators, the nontrivial topology is not related to invariants associated with completely filled bands but with ones associated with the Fermi surface. The Fermi surface of a topological metal consists of disconnected sheets, each enclosing a Weyl node, which is a point of contact between two nondegenerate bands. Such a point contact acts as a source of Berry curvature or a magnetic monopole in momentum space. Its charge, or the flux of the Berry curvature through the enclosing Fermi surface sheet, is a topological invariant. We review the current state of this rapidly growing field with a focus on bulk transport phenomena in topological metals.

1. INTRODUCTION

A significant part of modern condensed matter physics deals with macroscopic quantum phenomena, that is, direct manifestations of quantum mechanics, which naturally governs the behavior of matter on the atomic and subatomic scales, on macroscopic scales, which are, roughly speaking, the size scales discernible by the naked human eye. In many instances, e.g., in the case of perhaps the most well-known macroscopic quantum effect, the superconductivity, the underlying source of such phenomena is electron–electron interactions, which make the electrons behave cooperatively, leading to macroscopic quantum coherence. Interactions are not the only source of the macroscopic quantum coherent behavior, however. The integer quantum Hall effect (IQHE), which manifests in a precisely quantized transverse resistivity of a two-dimensional electron gas (2DEG) system in a strong perpendicular magnetic field, results from the interplay of two purely quantum phenomena, which do not involve interactions: localization of electrons in a random impurity potential and nontrivial topology of the single-electron eigenstates in the presence of magnetic field. The nontrivial topology leads to delocalized metallic edge states in an otherwise insulating sample, which is what ultimately results in the quantized Hall effect.

It is now well understood that macroscopic quantum behavior, brought about by the nontrivial electronic structure topology, is not limited to 2DEG in a strong perpendicular magnetic field. This new understanding started to emerge from the pioneering work of Haldane (1) and developed fully after the discovery of topological insulators (TIs) (2, 3) and the tremendous amount of work that followed. The most recent new development in this field is the realization that not only insulators but also metals may be topological. Although partially anticipated in earlier work (4–7), this idea was firmly established after the theoretical and later experimental discovery of Weyl and Dirac semimetals (8–20).

In a metal, nearly everything of observable consequence happens on the Fermi surface. Thus, in order for a metal to be topological, the corresponding momentum space invariant needs to be defined on the Fermi surface. This is in contrast to TIs, where topological invariants have to do with completely filled bands and thus involve all states in the first Brillouin zone (BZ). As it happens, the only topological invariant, that may be defined on the Fermi surface and leads to observable consequences, is the flux of what is known as the Berry curvature through the two-dimensional (2D) Fermi surface of a three-dimensional (3D) metal.

Berry curvature is a close analog of the magnetic field but is defined in momentum rather than real space. The Hamiltonian of noninteracting electrons in a crystal is a matrix $H(\mathbf{k})$, whose elements are labeled by the atomic orbital and spin quantum numbers and that depends on the crystal momentum $\mathbf{k}$ as a parameter. The electronic structure is defined by the eigenvalues and eigenvectors of the equation

$$H(\mathbf{k})|u(\mathbf{k})\rangle = \epsilon(\mathbf{k})|u(\mathbf{k})\rangle. \qquad 1.$$

Consider an overlap between a particular eigenvector taken at point $\mathbf{k}$ and the same eigenvector taken at a nearby point in momentum space $\mathbf{k} + \delta\mathbf{k}$:

$$\langle u(\mathbf{k})|u(\mathbf{k} + \delta\mathbf{k})\rangle \approx 1 + \delta\mathbf{k} \cdot \langle u(\mathbf{k})|\nabla_{\mathbf{k}}|u(\mathbf{k})\rangle \approx e^{i\mathbf{A}(\mathbf{k})\cdot\delta\mathbf{k}}, \qquad 2.$$

where $\mathbf{A}(\mathbf{k}) = -i\langle u(\mathbf{k})|\nabla_{\mathbf{k}}|u(\mathbf{k})\rangle$ is called the Berry connection. The curl of the Berry connection,

$$\boldsymbol{\Omega}(\mathbf{k}) = \nabla_{\mathbf{k}} \times \mathbf{A}(\mathbf{k}), \qquad 3.$$

is the Berry curvature. When the Berry curvature is not zero, the phase $\mathbf{A}(\mathbf{k}) \cdot \delta\mathbf{k}$ cannot be eliminated by a gauge transformation and has observable consequences.

Suppose we have a Fermi surface sheet with a nonzero flux of the Berry curvature through it. Gauss' theorem implies that there must then be a point source or sink of the Berry curvature

enclosed by this Fermi surface. In the vicinity of this point, the Berry curvature takes, up to trivial rescaling of the crystal momentum components, a universal form

$$\mathbf{\Omega}(\mathbf{k}) = \pm \frac{\mathbf{k}}{2k^3}, \qquad 4.$$

such that

$$C = \frac{1}{2\pi} \int \mathbf{\Omega}(\mathbf{k}) \cdot d\mathbf{S} = \pm 1. \qquad 5.$$

C is the Chern number, which is associated with any 2D Fermi surface sheet, enclosing a point source or sink of the Berry curvature and may be regarded as the topological charge of this point. The sign depends on whether the point is a source or a sink.

A point source or a sink of the Berry curvature is clearly some sort of a singularity of the electronic structure. As we see explicitly later, this singularity turns out to be a point of degeneracy between two bands. Such degeneracy points are called Weyl nodes (8). The name arises from the following important observation. Just as the Berry curvature in the vicinity of the degeneracy point takes a universal form of the magnetic field of a point monopole 4, the band Hamiltonian itself, when expanded near the degeneracy point, takes the following universal form as well:

$$H(\mathbf{k}) = \pm v_F \boldsymbol{\sigma} \cdot \mathbf{k}, \qquad 6.$$

where the crystal momentum $\mathbf{k}$ is measured from the degeneracy point, and we use $\hbar = c = 1$ units throughout, except in some of the final formulas. $\boldsymbol{\sigma}$ is a triplet of Pauli matrices, which act in the reduced Hilbert space of the two touching bands, and the sign in front is the topological charge of the node. This Hamiltonian is identical, up to a replacement of v_F by the speed of light c, to the Hamiltonian for massless relativistic fermions, proposed by Hermann Weyl in 1929. The topological charge of the band touching node is identical to the chirality of Weyl fermions, right-handed (R) corresponding to the topological charge $C = +1$ and left-handed (L) to $C = -1$.

Equation 6 betrays an important property of topological metals: Their band eigenstates must be nondegenerate. This requires either broken time-reversal symmetry (a magnetic material) or a broken spatial inversion symmetry (the crystal structure lacks a center of inversion). Otherwise, all bands are doubly degenerate because of the Kramers theorem. However, if either time-reversal or inversion are indeed broken, Equation 6 also makes it clear that no other conditions are necessary for the existence of the Weyl band touching nodes in a 3D material, because the three components of the crystal momentum provide the necessary three real parameters needed to make two band eigenstates coincide in energy. Thus Weyl nodes occur generically in any 3D magnetic or noncentrosymmetric material, of which there are plenty.

In this article, we review the exciting and rapidly developing subject of Weyl semimetals, focusing on response and transport phenomena. As excellent reviews of the experiments already exist (see, e.g., 21, 22), we instead focus on general principles presented using simple idealized model systems.

2. WEYL SEMIMETAL

The presence of Weyl nodes in the electronic structure is by itself of little interest. The important question is whether their presence leads to observable consequences. It is clear that such consequences will only exist when the nodes are close to the Fermi energy (Weyl metal), ideally right at the Fermi energy (Weyl semimetal). In addition, there should not be any other states at the Fermi energy, which may obscure the effects caused by the Weyl nodes. Although the presence of Weyl nodes somewhere in the band structure is guaranteed simply by broken time-reversal

or inversion symmetries and by the three dimensionality along with a nonvanishing spin-orbit interaction (these conditions lead to Berry curvature, which is generally nonzero everywhere in the first BZ), their location relative to the Fermi energy is not generally guaranteed by anything.

2.1. Weyl Semimetal Near the Quantum Hall Plateau Transition

For a given electron density, Pauli principle, which states that two electrons cannot occupy the same state, and the fact that every band has exactly the same number of states, equal to the number of unit cells in the crystal, fix the volume in the crystal momentum space, enclosed by the Fermi surface, modulo BZ volume. This statement is known as the Luttinger's theorem. Because the shape of the Fermi surface depends on the details of the band structure, it follows that the location of the Fermi energy is universally determined by the electron density and independent of other details only in insulators. This suggests, at least in theory, a route for finding a material with Weyl nodes at the Fermi energy: One needs to start from an insulator, which has the required broken time-reversal or inversion symmetry, and close its gap, i.e., tune the insulator to a quantum phase transition. The Fermi level in this case is pinned to the band touching points by the electron density. This is exactly the right strategy: Weyl semimetal, i.e., a material with Weyl nodes but no other states at the Fermi energy, occurs generically as an intermediate phase between two topologically distinct kinds of insulators, when a direct transition between them is impossible (7, 10). An important implication of this is that the most convenient way to describe Weyl semimetals theoretically is by expanding about such critical points. The simplest case of this occurs when time-reversal symmetry is violated, and the transition then is between an ordinary 3D insulator and a quantum anomalous Hall insulator with quantized Hall conductivity.

A 3D quantum anomalous Hall insulator may be obtained by making a stack of 2D quantum Hall insulators (23). 2D quantum anomalous Hall effect (QAHE) arises naturally in a very thin film of a 3D TI material doped with magnetic impurities (24, 25). A 3D time-reversal invariant TI is a bulk insulator with nontrivial electronic structure topology, which leads to gapless metallic surface states, described by a 2D massless Dirac Hamiltonian of the general form

$$H = v_{\mathrm{F}}(\hat{z} \times \boldsymbol{\sigma}) \cdot \mathbf{k}, \qquad\qquad 7.$$

where $\boldsymbol{\sigma}$ is the spin degree of freedom, and $\hat{z}$ is the normal to the surface. The gaplessness of the spectrum of Equation 7 is protected by time-reversal symmetry, which prohibits the mass term in the 2D Dirac Hamiltonian. If time-reversal symmetry is violated, which may be accomplished by doping the surface with magnetic impurities, the mass term will be allowed and a gap in the 2D Dirac surface state dispersion will be opened.

A thin film of magnetically doped 3D TI may be modeled by focusing only on the low-energy degrees of freedom, which are simply the 2D Dirac surface states of Equation 7 on the top and bottom surfaces of the film (see **Figure 1**). The corresponding Hamiltonian reads

$$H = v_{\mathrm{F}}\tau^z(\hat{z} \times \boldsymbol{\sigma}) \cdot \mathbf{k} + \Delta_{\mathrm{S}}\tau^x + b\sigma^z. \qquad\qquad 8.$$

Here the eigenvalues of τ^z refer to the top or bottom surface degree of freedom; $\hat{z}$ is the direction, perpendicular to the plane of the film; Δ_{S} is the probability amplitude for tunneling between the top and bottom surfaces of the film; and b is the exchange spin-splitting, which arises because of the presence of magnetized impurities. Note that $b\sigma^z$ acts as a "mass term" for the individual 2D Dirac surface states, as mentioned above. A simple similarity transformation $\sigma^{\pm} \to \tau^z\sigma^{\pm}$ and $\tau^{\pm} \to \sigma^z\tau^{\pm}$ brings this to the form

$$H = v_{\mathrm{F}}(\hat{z} \times \boldsymbol{\sigma}) \cdot \mathbf{k} + (\Delta_{\mathrm{S}}\tau^x + b)\sigma^z, \qquad\qquad 9.$$
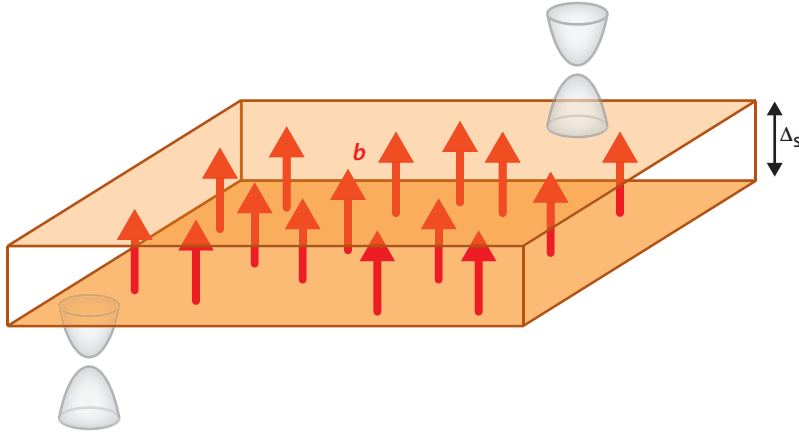
Figure 1

Thin film of magnetically doped 3D TI. Δ_S is the tunneling amplitude between the top and bottom 2D Dirac surface states, and b is the spin splitting caused by magnetized impurities. When $b > \Delta_S$, the film is a quantum anomalous Hall insulator with $\sigma_{xy} = e^2/h$. When $b < \Delta_S$, it is an ordinary insulator with zero Hall conductivity. Abbreviation: TI, topological insulator.

which may be further brought to a block-diagonal form by diagonalizing the $\Delta_S \tau^x$ matrix,

$$H_r = v_{\mathrm{F}}(\hat{z} \times \boldsymbol{\sigma}) \cdot \mathbf{k} + (b + r\Delta_S)\sigma^z, \qquad 10.$$

where $r = \pm$. Each of the 2×2 blocks of Equation 10 is the Hamiltonian of a 2D Dirac fermion with a mass $m_r = b + r\Delta_S$. The 2D Dirac fermion exhibits an interesting property, which is known as the parity anomaly (1, 26, 27). In our context this means that $H_\pm$ is associated with a Hall conductivity

$$\sigma_{xy}^r = \frac{e^2}{2h}\mathrm{sign}(m_r), \qquad 11.$$

when the Fermi energy is in the gap between the positive and negative energy bands, obtained by diagonalizing H_r,

$$\epsilon_{rs}(\mathbf{k}) = s\sqrt{v_{\mathrm{F}}^2\mathbf{k}^2 + m_r^2}, \qquad 12.$$

with $s = \pm$. The anomaly refers to the singular behavior of σ_{xy}^r in the limit $m_r \to 0$.

This implies that this system exhibits a quantum Hall plateau transition from $\sigma_{xy} = 0$ to $\sigma_{xy} = e^2/h$ as the ratio of b/Δ_S is varied and taking both b and Δ_S to be positive for concreteness. In other words, in two dimensions there exists a direct transition between a TI with $\sigma_{xy} = e^2/h$ and a normal insulator with $\sigma_{xy} = 0$. The critical point between the two is described by a massless 2D Dirac Hamiltonian.

Suppose we now make a stack of such 2D layers, exhibiting QAHE, as shown in **Figure 2**. Let individual layers be separated by insulating spacers, such that the amplitude for tunneling between the adjacent surfaces of neighboring QAHE layers is Δ_D, which we also take to be positive. We take the tunneling amplitude to beyond nearest-neighbor surface states to be negligibly small. The Hamiltonian that describes this system takes the form

$$H = v_{\mathrm{F}}\tau^z(\hat{z} \times \boldsymbol{\sigma}) \cdot \mathbf{k} + [\Delta_S + \Delta_D\cos(k_z d)]\tau^x - \Delta_D\sin(k_z d)\tau^y + b\sigma^z, \qquad 13.$$

where d is the period of the resulting superlattice heterostructure in the z direction. Making the same similarity transformation as above and partially diagonalizing the resulting Hamiltonian, we
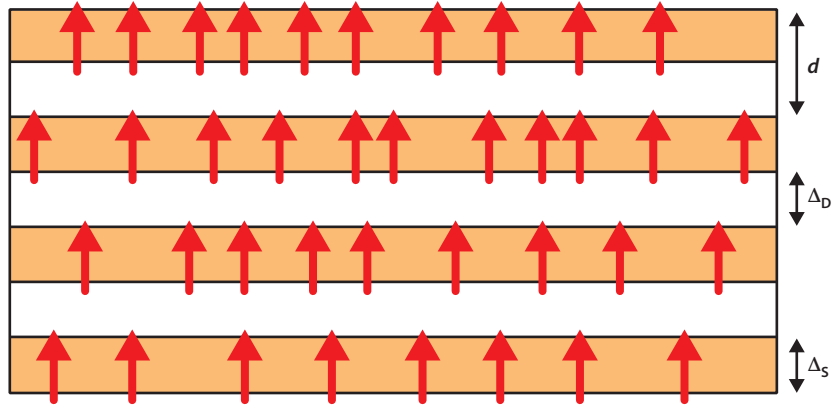
Figure 2

Coupled-layer construction of an elementary Weyl semimetal. Magnetically doped TI layers are coupled through insulating spacers. The tunneling amplitude between neighboring TI layers is Δ_D. Further-neighbor tunneling is assumed to be negligibly small, leading to a particle–hole symmetric electronic structure. Abbreviation: TI, topological insulator.

obtain

$$H_r = v_F(\hat{z} \times \boldsymbol{\sigma}) \cdot \mathbf{k} + m_r(k_z)\sigma^z, \qquad \text{14.}$$

where $m_r(k_z) = b + r\sqrt{\Delta_S^2 + \Delta_D^2 + 2\Delta_S\Delta_D \cos(k_z d)} \equiv b + r\Delta(k_z)$. Now, we see that the quantum Hall plateau transition we discussed before as a function of b/Δ_S may now happen "on its own" in momentum space as k_z is swept through the BZ. Indeed $m_-(k_z)$ changes sign at $k_z^{\pm} = \pi/d \pm k_0$, where

$$k_0 = \frac{1}{d} \arccos\left(\frac{\Delta_S^2 + \Delta_D^2 - b^2}{2\Delta_S\Delta_D}\right). \qquad \text{15.}$$

At $\mathbf{k} = (0, 0, k_z^{\pm})$, the two nondegenerate bands, corresponding to the eigenvalue $r = -$ touch each other; i.e., these are locations of two Weyl nodes (see **Figure 3**).
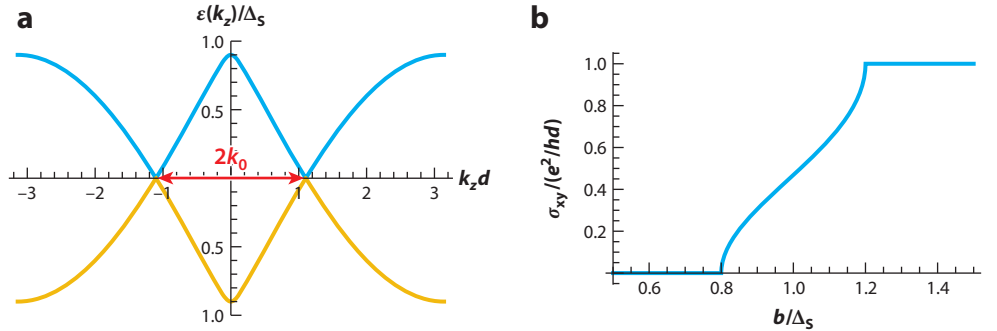

Figure 3

(*a*) Electronic structure of the simplest Weyl semimetal, with two nodes of opposite chirality, separated by a distance of $2k_0$ along the z axis in momentum space. (*b*) The corresponding anomalous Hall conductivity as a function of b/Δ_S, showing a broadened plateau transition. Weyl semimetal is an intermediate gapless phase between the quantum anomalous Hall and ordinary insulators.

Figure 4

Phase diagram of the magnetically doped multilayer structure. The width of the Weyl semimetal phase as a function of b/Δ_S vanishes in the limit of decoupled 2D layers, in which case a direct transition between an ordinary and a quantum anomalous Hall insulator exists. The maximal width is achieved once $\Delta_D/\Delta_S \geq 1$. Abbreviation: QAHE, quantum anomalous Hall effect.

The nodes exist as long as the spin splitting b is in the interval between two critical values $b_{c1} < b < b_{c2}$, where $b_{c1} = |\Delta_S - \Delta_D|$ and $b_{c2} = \Delta_S + \Delta_D$. When $b < b_{c1}$ the system is an ordinary insulator with $\sigma_{xy} = 0$, whereas when $b > b_{c2}$ it is a 3D quantum anomalous Hall insulator with $\sigma_{xy} = e^2/hd$. In between the heterostructure is the intermediate Weyl semimetal phase with

$$\sigma_{xy} = e^2 k_0/\pi h, \qquad\qquad 16.$$

which depends only on the distance between the Weyl nodes in momentum space and varies continuously between 0 and e^2/hd (see **Figure 4**). Thus, unlike in two dimensions, in three dimensions a direct transition between a TI with nonzero quantized Hall conductivity and a normal insulator with zero Hall conductivity does not exist. The transition instead proceeds through an intermediate gapless Weyl semimetal phase. The system, described above, constitutes the simplest potential realization, the "hydrogen atom" of Weyl semimetals. A lot of the general physical properties of Weyl semimetals may be understood by studying this system.

2.2. Weyl Semimetal from a 3D Dirac Semimetal

A distinct and a very useful viewpoint on Weyl semimetals is obtained in the limit when the range of the Weyl semimetal phase in the coupled-layer construction, described above, is maximized. This happens when $\Delta_D = \Delta_S$, i.e., when neighboring layers are coupled maximally strongly.

In this limit, when both time-reversal and inversion symmetries are present, i.e., when $b = 0$, Equation 13 describes a Dirac semimetal, a state in which doubly degenerate conduction and valence bands touch at the edge of the BZ $\mathbf{k} = (0, 0, \pi/d)$. This point is in fact a critical point between a time-reversal invariant topological and normal insulator in 3D. Close to this critical point, when the gap at $\mathbf{k} = (0, 0, \pi/d)$, $|\Delta_S - \Delta_D|$ is small, Weyl semimetal phase arises most easily, as long as $b > |\Delta_S - \Delta_D|$. The value of this limit from the theoretical viewpoint is universality and extra symmetry (essentially Lorentz invariance) that emerges. We discuss physics of Weyl semimetals by expanding on this ideal limit.

Note that this picture does not rely on any particular model of Weyl semimetal like the superlattice model introduced above. Indeed, let us consider a hypothetical material with four degrees of freedom per unit cell: two orbital and two spin. This is the minimal number of degrees of freedom necessary to obtain a pair of doubly degenerate bands, which may exhibit a gap-closing quantum phase transition. Let us introduce two sets of Pauli matrices τ^i and σ^i to represent operators acting on the orbital and spin degrees of freedom correspondingly. In the presence of inversion symmetry, the two orbital states may always be chosen to be related to each other by the parity operator P. We thus take the orbital states to be the eigenstates of τ^z, in which case the parity operator $P = \tau^x$.

The most general time-reversal and parity-invariant momentum-space Hamiltonian, describing the above system, may be written as (28)

$$H(\mathbf{k}) = d_0(\mathbf{k}) + \sum_{a=1}^{5} d_a(\mathbf{k})\Gamma^a, \tag{17}$$

where Γ^a are the five matrices, realizing the Clifford algebra $\{\Gamma^a, \Gamma^b\} = 2\delta^{ab}$, even under the product of parity and time reversal $P\Theta$. The five Γ matrices are given by

$$\Gamma^1 = \tau^x, \ \Gamma^2 = \tau^y, \ \Gamma^3 = \tau^z\sigma^x, \ \Gamma^4 = \tau^z\sigma^y, \ \text{and} \ \Gamma^5 = \tau^z\sigma^z. \tag{18}$$

It is clear that Γ^1 is even under both parity and time reversal separately while Γ^{2-5} are odd under both separately. The eigenvalues of Equation 17 form two pairs of doubly degenerate bands

$$\epsilon_{\pm}(\mathbf{k}) = d_0(\mathbf{k}) \pm \sqrt{\sum_{a=1}^{5} |d_a(\mathbf{k})|^2}. \tag{19}$$

The two pairs of bands may be forced to touch at a crystal symmetry related set of time-reversal invariant momenta (TRIM) $\mathbf{\Gamma}$. In this case, we have $d_{2-5}(\mathbf{\Gamma}) = 0$ automatically, whereas $d_1(\mathbf{\Gamma}) \equiv m$ needs to be tuned to zero if no additional symmetries are present. Because d_{2-5} are all odd under parity, their Taylor expansions near $\mathbf{\Gamma}$ will generically start from linear terms, whereas the expansion of $d_{0,1}(\mathbf{k})$ will start from a constant and continue with a quadratic term. Then the momentum space Hamiltonian Equation 17, expanded to leading order near TRIM $\mathbf{\Gamma}$, takes the following form:

$$H(\mathbf{k}) = \gamma^0\gamma^i k_i + m\gamma^0, \tag{20}$$

where $\gamma^0 \equiv \Gamma^1$, whereas the other three Dirac matrices γ^i are defined by this expansion. We have absorbed the velocity coefficients into the definition of the momentum components k_i, which are measured from $\mathbf{\Gamma}$, and taken $d_0(\mathbf{\Gamma})$ to define the overall zero of energy. In the case of the superlattice model, the Dirac point occurs at $\mathbf{\Gamma} = (0, 0, \pi/d)$ when $\Delta_S = \Delta_D$ and $m = \Delta_S - \Delta_D$. The gamma matrices in this case are given by $\gamma^0 = \tau^x$, $\gamma^1 = i\tau^y\sigma^y$, $\gamma^2 = -i\tau^y\sigma^x$, and $\gamma^3 = i\tau^z$.

The utility of this "relativistic" representation of the Hamiltonian, apart from emphasizing a connection to the relativistic quantum mechanics and the emergent Lorentz invariance, is that

we may now easily classify time-reversal and inversion symmetry breaking perturbations to H in terms of the Γ matrices and their descendants and clearly see their physical meaning. The ten possible perturbations to H are

$$\gamma^0 \gamma^\mu \gamma^5 \text{ and } \gamma^0 \sigma^{\mu\nu}, \qquad 21.$$

where $\sigma^{\mu\nu} = (i/2)[\gamma^\mu, \gamma^\nu]$; $\mu, \nu = 0, 1, 2, 3$; and $\gamma^5 = i\gamma^0\gamma^1\gamma^2\gamma^3$ is the chirality operator. The significance of γ^5 is that the operator,

$$P = \frac{1}{2}(1 + \gamma^5), \qquad 22.$$

projects out the two Weyl fermion components of the Dirac fermion. The right-handed Weyl fermion corresponds to the eigenvalue $+1$ of γ^5, whereas the left-handed Weyl fermion corresponds to the eigenvalue -1.

Of the 10 perturbations in Equation 21, there are 6 that are odd under time-reversal symmetry but even under parity: $\gamma^0\gamma^i\gamma^5$ and $\gamma^0\sigma^{ij}$; and 4 that are even under time reversal but odd under parity: γ^5 and $\gamma^0\sigma^{0i}$. In other words, $\gamma^0\gamma^i\gamma^5$ transforms as an axial current vector; γ^5 is a pseudoscalar; $\gamma^0\sigma^{ij}$ transforms as magnetization, perpendicular to the ij plane; and $\gamma^0\sigma^{0i}$ transforms as electric polarization along the i axis. As a result, perturbation of the type $\mathbf{b} \cdot \gamma^0 \boldsymbol{\gamma} \gamma^5$ acts as a chiral vector potential, shifting the location of Weyl fermions of different chirality to different momenta, i.e., precisely creating a Weyl semimetal. A $b_0\gamma^0\gamma^0\gamma^5 = b_0\gamma^5$ term acts as a time component of the chiral gauge field, shifting the two Weyl components of the Dirac fermion to different energies. The term of the type $b_i\epsilon_{ijk}\gamma^0\sigma^{jk}$ creates nodal lines, in the plane, perpendicular to the vector $\mathbf{b}$. Finally, a $b_i\gamma^0\sigma^{0i}$ term, which breaks inversion symmetry, creates Weyl nodes, which in this case come in multiples of four (29) (to obtain these, the inclusion of terms that are higher order in momentum and break the continuous rotational symmetry of the low-energy Dirac Hamiltonian Equation 20 down to a discrete crystal symmetry is necessary).

3. TRANSPORT IN WEYL METALS

Perhaps the most important consequence of the nontrivial electronic structure topology is that it may lead to unique transport and more generally response to external probes. A famous example of this is the quantized Hall conductivity of a 2D quantum Hall insulator, described in Section 2.1. This quantization is a consequence of the fact that the transport in a quantum Hall insulator occurs entirely in the one-dimensional (1D) chiral edge states. Because the branches of different chirality are separated to opposite edges of a macroscopic sample, no scattering between them is possible. This means that chiral charges, corresponding to the edge states, are separately conserved, which leads to universal quantized transport.

In this section, similar ideas are applicable to bulk transport in Weyl semimetals. This is a consequence of the (approximate) separate conservation of the number of electrons of different chirality, which becomes most precise in the vicinity of the 3D Dirac critical point, described in Section 2. These (quasi-)universal transport phenomena in Weyl metals may be regarded as being a consequence of chiral anomaly, a well-known and important phenomenon in particle physics (30, 31), which has now found its way into condensed matter.

3.1. Chiral Anomaly

Chiral anomaly refers to nonconservation of chiral charge for massless relativistic particles, when conservation is naïvely expected based on symmetry. Indeed, consider the Dirac Hamiltonian

Equation 20 in the limit when the mass $m = 0$:

$$H(\mathbf{k}) = \gamma^0 \gamma^i k_i. \qquad 23.$$

From the anticommutation property of the individual gamma matrices, it immediately follows that the γ^5 matrix commutes with the Hamiltonian,

$$[H, \gamma^5] = 0. \qquad 24.$$

This expresses an exact extra conservation law that exists for massless relativistic fermions: conservation of the chiral charge. This conservation law implies that the chiral current, defined by $j_5^\mu = \psi^\dagger \gamma^0 \gamma^\mu \gamma^5 \psi$, where $\psi^\dagger$ is the electron creation operator, must satisfy the continuity equation,

$$\partial_\mu j_5^\mu = 0, \qquad 25.$$

which must hold in addition to the regular electric charge conservation law,

$$\partial_\mu j^\mu = 0, \qquad 26.$$

where $j^\mu = \psi^\dagger \gamma^0 \gamma^\mu \psi$. In reality, the seemingly obvious chiral charge conservation turns out to be violated in the second-quantized theory, when the negative-energy Dirac sea is filled with electrons, in the presence of an applied electromagnetic field

$$\partial_\mu j_5^\mu = \frac{e^2}{16\pi^2} \epsilon^{\mu\nu\alpha\beta} F_{\mu\nu} F_{\alpha\beta} = \frac{e^2}{2\pi^2} \mathbf{E} \cdot \mathbf{B}. \qquad 27.$$

The simplest way to understand this is to consider a massless Dirac fermion, described by Equation 23, in the presence of a constant magnetic field, applied in, say, the z direction. The resulting Landau level structure for the two independent Weyl fermion components is shown in **Figure 5**. Most importantly, the chirality of the Weyl fermions is reflected in their Landau level spectrum, manifesting in the presence of a special Landau level in each case, whose dispersion is given by

$$\epsilon(k_z) = \pm k_z, \qquad 28.$$

where the sign in front is minus the chirality (eigenvalue of the γ^5 matrix) of the corresponding Weyl fermion. Suppose we now apply an electric field $\mathbf{E}$ in the same direction as the magnetic field. The electrons are accelerated at a rate eE, in the $\hat{E}$ direction (we imagine electrons to be positively charged for the sake of this argument, just to avoid some awkward minus signs; the final result is independent of the sign of the charge), which, due to the presence of the chiral Landau levels, results in the following rates of the right- and left-handed charge generation:

$$\frac{\partial n_{\mathrm{R,L}}}{\partial t} = \pm \frac{e^2}{4\pi^2} \mathbf{E} \cdot \mathbf{B}, \qquad 29.$$

where the factor of $eB/4\pi^2$ arises from the density of states of the chiral Landau levels. This precisely corresponds to Equation 27, with $j_5^0 \equiv n_5 = n_{\mathrm{R}} - n_{\mathrm{L}}$.

This may seem fairly inconsequential as the chiral charge by itself is not a directly observable quantity. To see that the chiral anomaly does in fact have observable consequences, it is useful to note that Equation 27 may be obtained from the following action for the electromagnetic field:

$$S = -\frac{e^2}{4\pi^2} \int dt \, d^3r \, b_\mu \epsilon^{\mu\nu\alpha\beta} A_\nu \partial_\alpha A_\beta. \qquad 30.$$

Here b_μ are components of the chiral gauge field, which couples linearly to the chiral current as $b_\mu j_5^\mu$, just as ordinary gauge field couples linearly to the ordinary electric current as $A_\mu j^\mu$. Equation 27 is obtained by calculating the functional derivative of S with respect to the chiral gauge field b_μ, which gives the chiral current j_5^μ, and taking the divergence.
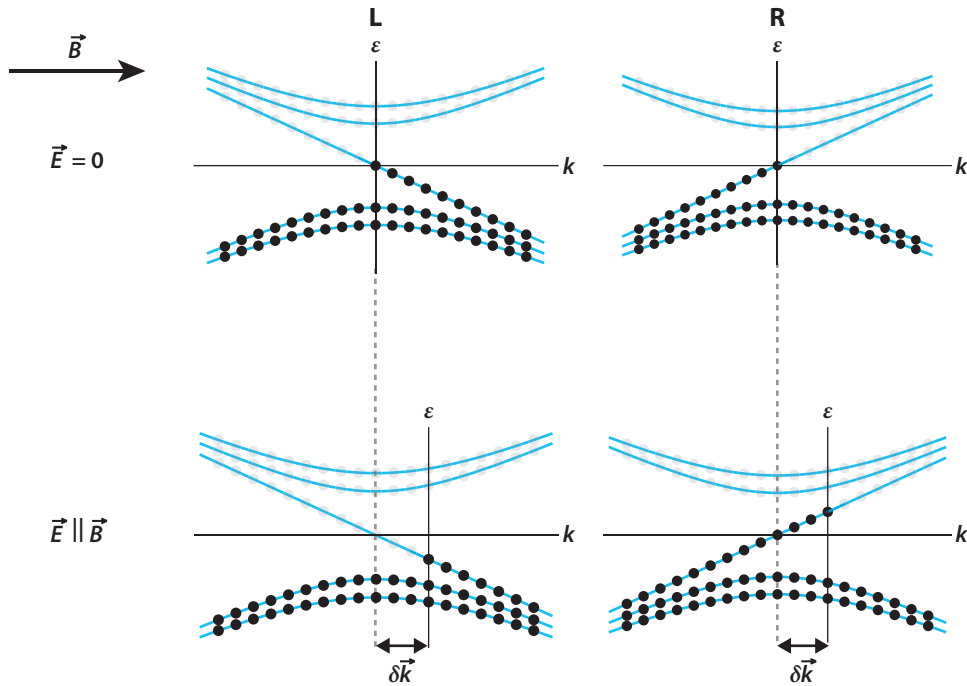
Figure 5

Illustration of the chiral anomaly, based on a Landau level spectrum of Weyl fermions in an external magnetic field. (Top panel) Energy spectrum of the left-handed (L) and right-handed (R) fermions in equilibrium in the presence of a magnetic field $\vec{B}$. Filled states with negative energy are shown by black dots, whereas empty states with positive energy are shown by gray dots. (Bottom panel) Same spectrum, but in the presence, in addition, of an electric field $\vec{E}$, parallel to the magnetic field $\vec{B}$. All states have been displaced in momentum space by an amount $\delta \vec{k} \sim -\vec{E}$ from their equilibrium locations. As a consequence, right-handed particles and left-handed antiparticles have been produced.

Equation 30 corresponds to the famous triangle diagram (shown in **Figure 6**), which is a diagram with three vertices; two vertices correspond to the ordinary charge current j^μ and one to the chiral current j_5^μ. The original discovery of the chiral anomaly by Adler (30) and by Bell & Jackiw (31) in 1969 was made when evaluating this diagram in the context of the problem of neutral pion decay into two photons,

$$\pi^0 \to 2\gamma. \qquad \qquad 31.$$

This process, which naïvely should be very slow owing to small masses of the quarks (pion is a quark–antiquark pair), in fact is very fast, leading to the neutral pion lifetime being many orders of magnitude smaller than that of the two charged pions. The explanation for this turned out to be the chiral anomaly, which now, almost 50 years later, has found its way into condensed matter physics as well.

The importance of Equation 30 stems from the fact that it clearly has a topological origin, as it contains gauge fields, coupled through the fully antisymmetric tensor and multiplied by a universal coefficient. One may thus expect the corresponding response to be robust and detail independent, which is always of great interest, and of potential technological importance. In the following section, we describe these universal electromagnetic response phenomena, resulting from the chiral anomaly, as applicable to Weyl metals.
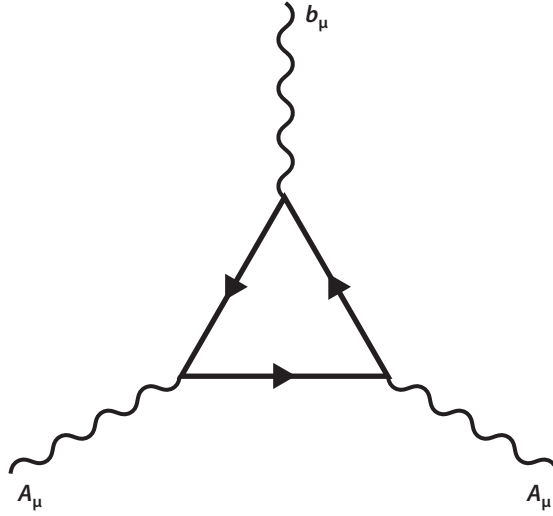
Figure 6

Graphical representation of Equation 30, known as the triangle diagram. The three vertices correspond to the chiral current (*top vertex*) and two ordinary electrical currents (*bottom vertices*).

3.2. Chiral Anomaly and Transport in Weyl Metals

To see the observable consequences of the chiral anomaly, we may vary the action S with respect to the electromagnetic gauge fields A_μ. This gives the following expression for the chiral anomaly contribution to the measurable charge current:

$$j^\nu = \frac{e^2}{2\pi^2} b_\mu \epsilon^{\mu\nu\alpha\beta} \partial_\alpha A_\beta. \qquad 32.$$

Suppose the chiral gauge field b_μ has both spatial and temporal components $b_\mu = (b_0, -\mathbf{b})$. Then we obtain

$$\mathbf{j} = \frac{e^2}{2\pi^2} (\mathbf{E} \times \mathbf{b}) \qquad 33.$$

and

$$\mathbf{j} = \frac{e^2}{2\pi^2} b_0 \mathbf{B}. \qquad 34.$$

To understand the meaning of Equations 33 and 34, we first need to understand the physical meaning of the chiral gauge field b_μ in the condensed matter context. Suppose we add a term $b_\mu j_5^\mu$ to the Dirac Hamiltonian Equation 20:

$$H(\mathbf{k}) = \gamma^0 \gamma^i (k_i - b_i \gamma^5) + m\gamma^0 + b_0 \gamma^5. \qquad 35.$$

It is then clear that, when $m = 0$, the chiral gauge field simply shifts the two Weyl fermion components of the massless Dirac fermion to different locations in momentum space ($\mathbf{b}$) or in energy (b_0). In particular, a nonzero $\mathbf{b}$ creates a Weyl semimetal, in which two Weyl fermions are separated by $2|\mathbf{b}|$ in momentum space along the direction of the vector $\mathbf{b}$ in momentum space. Chiral anomaly in this context means that, though naïvely the separation between the Weyl nodes may be eliminated by a chiral gauge transformation

$$\psi \to e^{i\gamma^5 \theta} \psi, \quad b_\mu \to b_\mu + \partial_\mu \theta, \qquad 36.$$

where $\partial_\mu\theta = -b_\mu$, in reality this is impossible: The chiral transformation leaves behind precisely the topological term of Equation 30. The mass term $m\gamma^0$ violates the chiral gauge invariance explicitly. However, gapless Weyl points still exist as long as $|\mathbf{b}| > m$, separated in momentum space by $2\sqrt{\mathbf{b}^2 - m^2}$. Chiral gauge invariance is then effectively restored in the limit $|\mathbf{b}| \gg m$.

An observable consequence of the momentum-space separation between the Weyl nodes is the topological current, given by Equation 33. This describes the anomalous Hall effect (AHE) with the transverse conductivity given by

$$\sigma_{xy} = \frac{e^2}{h}\frac{2|\mathbf{b}|}{2\pi}, \qquad\qquad 37.$$

which is exactly Equation 16 that we obtained before based on analogy with the quantum Hall plateau transition. We thus see that AHE in magnetic Weyl semimetals may be regarded as being a consequence of chiral anomaly.

This is not simply a rederivation of Equation 16, however, as Equation 37, being a consequence of the chiral anomaly, implies significantly more universality of this result than may naïvely be expected. Indeed, a quantized value of the transverse conductivity of a quantum Hall insulator is protected by the spectral gap. As long as the Fermi energy is within the gap (which may be a mobility gap only), the quantized value of the Hall conductivity cannot change. This is not the case in a gapless system, such as a Weyl semimetal. Uncontrollable impurities and other imperfections will always shift the location of the Fermi energy, even if it exactly coincides with the Weyl nodes in a perfect stoichiometric sample. In general, we may thus expect bulk states to contribute to the Hall conductivity, and the universal (in the sense of being dependent only on the Weyl node separation) result of Equations 16 and 37 will not hold. It turns out, however, that Equation 37 is in fact much more robust than would normally be expected, which may be thought of as a consequence of the nonrenormalization of the chiral anomaly.

The universal topological result for the action, describing the electromagnetic response, Equation 30, holds as long as the field b_μ, which couples to the chiral current as $b_\mu j_5^\mu$, enters the Hamiltonian as a chiral gauge field, with nothing violating chiral gauge invariance except the chiral anomaly itself. Anything that explicitly violates chiral gauge invariance, i.e., the mass term $m\gamma^0$, or any term, containing higher powers of momentum in the Hamiltonian Equation 35, will produce nonuniversal corrections to Equation 30. The reverse is true as well: Anything that does not violate chiral gauge invariance, e.g., scalar (i.e., independent of the orbital and spin indices on which the gamma matrices are acting) impurity scattering potential, electron–electron interactions, deviation of the electron density from stoichiometry, etc., will not change the action, and the topological currents, obtained from it. This is somewhat similar to the universality of the Luttinger liquid physics in 1D systems, which may also be thought of as a consequence of the chiral anomaly (32).

Let us now shift our attention to the second kind of topological current that follows from the chiral anomaly, given by Equation 34. This equation describes a current, driven by an applied magnetic field and the chiral scalar potential b_0, which shifts the energies of the Weyl fermions in opposite directions depending on their chirality. This is quite troubling, because such an energy difference may exist even in equilibrium, if, for example, both time-reversal and inversion symmetry are violated (33). Equation 34 would then seem to imply an equilibrium current driven by an applied magnetic field, which certainly is not possible (34). In fact, such an equilibrium current would be possible if the Weyl fermions were realized as edge states on a 3D boundary of a four-dimensional (4D) quantum Hall insulator (35). In this case the edge states of a 4D quantum Hall insulator slab are precisely the two 3D Weyl fermions of opposite chirality, existing on the "top" and "bottom" surfaces of the slab. Applying a voltage V between the two surfaces and a

constant magnetic field parallel to the surface would lead precisely to an equilibrium current given by

$$\mathbf{j} = \frac{e^2}{2\pi^2} e V \mathbf{B},$$

38.

which is the 4D analog of the 2D quantized Hall current (also an equilibrium current). What makes an equilibrium current possible in both cases is the spatial separation of the 1D or 3D chiral fermions to opposite sides of a macroscopic sample. This makes it possible for the two chiral fermions to be in equilibrium independently from each other and at distinct chemical potentials, which leads to an equilibrium current.

In a bulk 3D Weyl metal, however, the Weyl fermions are separated in momentum rather than real space and cannot be in equilibrium at different chemical potentials independently from each other. Thus Equation 34 may only describe the low-frequency limit of a dynamical nonequilibrium response (36). This is best handled within the framework of the density response theory.

3.3. Anomalous Density Response in Weyl Metals

We start this section by reminding the reader fundamentals of the density response in a metal. Although the response at short length-scales and timescales is highly complicated and nonuniversal, it becomes very simple and universal on large length-scales and timescales, much longer than the scattering time τ and the mean free path $\ell = v_F \tau$. Only conserved quantities are important in this limit, and their response is governed by simple hydrodynamic equations, which involve only the leading-order temporal and spatial derivatives. The only conserved quantity in a typical metal is the charge density, which obeys the diffusion equation

$$\frac{\partial n}{\partial t} = D \mathbf{\nabla}^2 (n + gV).$$

39.

Here n is the electron density, $D \sim v_F \ell$ is the diffusion coefficient, g is the density of states at the Fermi energy, and V is the external electrostatic potential. The two terms on the right-hand side of the diffusion equation correspond to two contributions to the electric current, diffusion and drift:

$$\mathbf{j} = e D \mathbf{\nabla} n + e g D \mathbf{\nabla} V = e D \mathbf{\nabla} n + \sigma \mathbf{E},$$

40.

where we have taken account of the Einstein relation $\sigma = e^2 g D$, which connects conductivity and the diffusion coefficient. By Fourier transforming Equation 40, we obtain the following expression for the density response function:

$$\chi(\mathbf{q}, \omega) = \frac{n(\mathbf{q}, \omega)}{V(\mathbf{q}, \omega)} = -g \frac{D\mathbf{q}^2}{D\mathbf{q}^2 - i\omega}.$$

41.

A characteristic feature of this response function is the "diffusion pole" at $i\omega = D\mathbf{q}^2$, which arises fundamentally from the particle number conservation. An important property of the response function, which can be seen from Equation 41, is that $\chi(\mathbf{q}, 0) = -g$. $\chi(\mathbf{q}, 0)$ describes equilibrium redistribution of the charge density in response to an applied inhomogeneous external potential. This means that the combination $n + gV$, which appears on the right-hand side of the diffusion Equation 39, has the meaning of a nonequilibrium part of the charge density.

Weyl metals are distinguished from ordinary metals by the emergence of an extra conserved quantity, the chiral charge, which in the simplest case of two Weyl nodes may be thought of as the difference between the densities of the right-handed and left-handed fermions. Chiral anomaly also implies that in the presence of an external magnetic field the chiral and the ordinary electric charge are coupled. The density response function is then a 2×2 matrix (37, 38), and the corresponding

transport equations read as

$$\frac{\partial n}{\partial t} = D\nabla^2(n + gV) + \Gamma\mathbf{B} \cdot \nabla(n_c + gV_c),$$

$$\frac{\partial n_c}{\partial t} = D\nabla^2(n_c + gV_c) - \frac{n_c + gV_c}{\tau_c} + \Gamma\mathbf{B} \cdot \nabla(n + gV). \qquad 42.$$

Here $\Gamma = e/2\pi^2 g$ is a new transport coefficient, characterizing Weyl metals, which describes the coupling between the chiral and the electric charge, induced by the chiral anomaly. Note that

$$eg\Gamma\mathbf{B} \cdot \nabla V = \frac{e^2}{2\pi^2}\mathbf{E} \cdot \mathbf{B}, \qquad 43.$$

which is identical to the right-hand side of Equation 27. This means that the chiral anomaly is nonrenormalized even in the diffusive transport regime at finite electron density and in the presence of impurity scattering. τ_c is the relaxation time for the chiral charge. The presence of a relaxation term in Equation 42 reflects the fact that the chiral charge in a Weyl metal is never exactly conserved. Its approximate conservation is an emergent low-energy property, which holds when the Fermi energy is close to the band-touching nodes. In this regime the chiral relaxation time is very long. For the multilayer model, described in Section 2, it is given by

$$\frac{1}{\tau_c} \sim \frac{\epsilon_F^2}{\Delta_S^2 \tau}, \qquad 44.$$

where ϵ_F is the Fermi energy. In general, Δ_S is a parameter of the order of the bandwidth. Note that the smallness of the chiral relaxation rate is not a consequence of separation between the Weyl fermions in momentum space but rather of orthogonality of their wavefunctions (in a sense, separation in Hilbert space), which arises due to the emergent conservation of chirality. Finally, V_c is the "chiral electrostatic potential," i.e., an external potential, which couples linearly to the chiral charge.

Because the electric charge is strictly conserved, the first of Equation 42 must have the form of a continuity equation. This immediately implies the following expression for the electric current in a Weyl metal:

$$\mathbf{j} = e D\nabla(n + gV) + e\Gamma(n_c + gV_c)\mathbf{B}. \qquad 45.$$

The first term in Equation 45 represents the standard diffusion and drift contributions to the electric current. The second term is due to the chiral anomaly and represents a contribution to the electric current, proportional to the nonequilibrium chiral charge density $n_c + gV_c$ and to the applied magnetic field

$$\mathbf{j}_{CME} = e\Gamma(n_c + gV_c)\mathbf{B}. \qquad 46.$$

This arises entirely from the chiral lowest Landau level and is known as the chiral magnetic effect (CME) (39, 40). This is precisely equivalent to the second topological current, arising from the chiral anomaly, given by Equation 35, if we identify $b_0 = (n_c + gV_c)/g$. Unlike Equation 35, however, which naïvely could be interpreted as predicting an equilibrium current, Equation 46 explicitly contains only a nonequilibrium part of the chiral charge density.

An important property of the coupled transport Equation 42 is that they contain several distinct length scales, which leads to complex non-Ohmic scale dependence of the sample conductance. This complex scale dependence is a unique feature of Weyl metals and is a macroscopic manifestation of the chiral anomaly. The first fundamental length scale in a Weyl metal is a magnetic-field-induced length scale

$$L_m = \frac{D}{\Gamma B}. \qquad 47.$$

Note that this is distinct from the magnetic length $\ell_B = 1/\sqrt{eB}$. The physical meaning of this new field-induced length scale will become clear below. The second important length scale is the chiral charge diffusion length

$$L_c = \sqrt{D\tau_c}. \tag{48}$$

To understand the role the two length scales play in transport, we solve Equation 42, assuming a cubic sample of volume L^3 and taking magnetic field to be aligned with the current for simplicity. One obtains the following expression for the scale-dependent conductance (41):

$$G(L) = \frac{e^2 N_\phi}{2\pi} f\left(\frac{L}{L_m}, \frac{L}{L_c}\right), \tag{49}$$

where $N_\phi = L^2/2\pi\ell_B^2$ is the number of flux quanta, penetrating a cross section of the sample, perpendicular to the direction of the magnetic field, which is also the same as the number of states in the lowest Landau level. The scaling function $f(x, y)$ is given by

$$f(x, y) = \frac{(1 + y^2/x^2)^{3/2}}{\frac{y^2}{2x}\sqrt{1 + y^2/x^2} + \tanh\left(\frac{x}{2}\sqrt{1 + y^2/x^2}\right)}. \tag{50}$$

When $L_m \gg L_c$, or equivalently $x \ll y$, the magnetic field has only a negligible effect on the conductance, and the scaling function has simple asymptotics

$$f(x, y) \approx \frac{2}{x}; \tag{51}$$

Equation 49 then gives the usual Ohmic conductance

$$G(L) = e^2 g D L. \tag{52}$$

Magnetoconductance is strong in the opposite limit when $L_m \ll L_c$ (however, we still assume quasiclassical condition $k_F \ell_B \gg 1$ holds), or when $x \gg y$. In this regime the scaling function simplifies to

$$f(x, y) \approx \frac{1}{\frac{y^2}{2x} + \tanh(x/2)}. \tag{53}$$

For $L < L_c$ this exhibits a crossover from the diffusive $L < L_m$ regime with regular Ohmic conductance given by Equation 52 to quasiballistic conductance when $L > L_m$,

$$G(L) = \frac{e^2 N_\phi}{2\pi}, \tag{54}$$

which is the conductance of an effective 1D system with N_ϕ conduction channels. Physically, this corresponds to a regime in which the conductance is dominated by the chiral lowest Landau level. Upon further increase of the sample size, a crossover back into the diffusive regime happens when $y^2 > x$ or equivalently when the sample size exceeds yet another distinct length scale

$$L > L_* = \frac{L_c^2}{L_m} \gg L_c. \tag{55}$$

The new length scale L_* may be obtained from equating the number of states in a sample of volume L_*^3 in the energy interval $1/\tau_c$, which is given by $g L_*^3/\tau_c$, to the number of states in the lowest Landau level N_ϕ. In this regime the conductance is dominated by the field-dependent chiral anomaly contribution but with $\propto B^2$, instead of $\propto B$, dependence

$$G(L) = \frac{e^4 \tau_c B^2}{4\pi^4 g} L \equiv \chi B^2 L. \tag{56}$$

When $L_m > L_c$ this result still holds in the infinite sample limit but with Equation 56 only representing a subdominant correction to the Ohmic conductance. It is quite remarkable that Equation 42 gives rise to such a rich and nontrivial scaling behavior of the conductance with three distinct length scales!

Generalizing Equation 56 to an arbitrary field direction, we obtain the expression for the longitudinal magnetoconductivity that was obtained originally implicitly in the limit of an infinite sample size (37, 38, 42),

$$\Delta\sigma_{xx} = \chi B^2 \cos^2\theta, \qquad 57.$$

where θ is the angle between the current and the magnetic field. Similar phenomena are also expected theoretically and observed in thermoelectric transport (43–46).

In fact, things are a bit more complex than Equation 57 predicts in a finite sample with boundaries (47). Indeed, suppose current is fed into the sample in the x direction, and the magnetic field is rotated in the xy-plane. Then, assuming an infinite sample in the x direction, we have

$$\sigma E_x + \chi(E_x B_x + E_y B_y)B_x = j_x,$$
$$\sigma E_y + \chi(E_x B_x + E_y B_y)B_y = 0. \qquad 58.$$

This implies that once the magnetic field is rotated away from the x direction, i.e., from perfect alignment with the current, chiral anomaly leads to the development of a transverse (with respect to the direction of the current) electric field

$$E_y = -\frac{\chi B_x B_y}{\sigma + \chi B_y^2} E_x. \qquad 59.$$

This, in turn, affects longitudinal conductivity, decreasing it compared with Equation 57. Substituting Equation 59 into the first of Equation 58, we obtain (47)

$$\Delta\rho_{xx}^{-1} = \frac{\sigma \chi B_x^2}{\sigma + \chi B_y^2}. \qquad 60.$$

This means that the angular dependence of the negative magnetoresistance signal is in fact stronger than implied by Equation 57. Instead of the $\cos^2\theta$ dependence, we have a Lorentzian at small angles, with the angular width

$$\Delta\theta \sim \sqrt{\frac{\sigma}{\chi B^2}}. \qquad 61.$$

This angular narrowing of the negative magnetoresistance is in fact observed experimentally (48, 49).

Another important consequence of the anomalous density response, described by Equation 42, is the existence of nonlocal transport phenomena (50), which are somewhat similar to the ones observed in graphene (51). This also follows from the fact that the chiral charge diffusion length L_c is a macroscopic length scale in Weyl metals. When L_c is large, nonequilibrium chiral charge, created by current in the presence of an applied magnetic field in one part of the sample, leads to voltage in response to an applied magnetic field far away from the current path. This is similar to the generation of voltage, transverse to the direction of the current, described by Equation 59, but in addition involves diffusion of the nonequilibrium chiral charge $n_c \sim \chi(\mathbf{E} \cdot \mathbf{B})$ over macroscopic distances $\sim L_c$.

4. CONCLUSIONS AND OUTLOOK

We have reviewed the current understanding of bulk topological transport phenomena in Weyl metals, focusing on general principles rather than specifics of particular materials. Some important topics have been left out of this review, in particular the interplay of bulk and surface state (Fermi arc) transport (52–54); transport in inhomogeneous Weyl metals, in which an extra contribution to the anomalous transport, related to the "chiral magnetic field" (curl of the chiral gauge field) is predicted to exist (55–58); and type-II Weyl semimetals (59).

The significance of the transport phenomena in Weyl metals, related to the chiral anomaly, is that these represent new observable macroscopic quantum phenomena. This is particularly clear from the highly nontrivial non-Ohmic scaling behavior of the conductance, described in Section 3. One may compare this with the nontrivial conductance scaling that arises because of quantum interference phenomena, which lead to Anderson localization (60), which is also a macroscopic quantum effect. However, an important difference is that, though localization phenomena can only be observed in small samples at very low temperatures, the anomalous transport phenomena in Weyl metals survive up to high temperatures, on the order of 100 K (48, 49), and exist in macroscopic samples.

An obvious question for future work is whether there are other manifestations of the chiral anomaly, which go beyond transport phenomena, described in this article. A promising candidate is the magnetic response. This is likely to be nontrivial in Weyl semimetals because of both the Landau level structure, which will give rise to anomalies in orbital response, and the spin-momentum locking, which is certain to affect the Pauli paramagnetic response. Interesting anomalies in magnetic response have in fact already been observed in one Weyl semimetal representative, NbAs (61).

Another area of interest is the interplay of electron–electron interactions and the nontrivial topology of the Weyl nodes. Some progress in this area has already been made. An incomplete list of topics that have been addressed include the following: the interplay of the chiral anomaly and spin and charge collective modes in Weyl metals (62–65), Luttinger liquid physics within the lowest chiral Landau level (66), potential strong correlation effects in Weyl semimetals (67, 68), and hydrodynamics in ultraclean Weyl metals (46). The interplay of superconductivity and topology of Weyl fermions is also of significant interest (69–75) owing to the potential for topological superconductivity with Majorana edge states. In particular, superconductivity in magnetic Weyl semimetals is necessarily topologically nontrivial (69, 73, 74), because the Berry curvature flux through the Fermi surface, felt by the Cooper pairs, forces point nodes to appear in the superconducting gap function (73, 74). The node projections on the surface BZ are then connected by Majorana arc edge states, which is in close analogy to how the Fermi arcs connect projections of the Weyl nodes.

On the experimental front, there is a clear need for better Weyl semimetal materials, which means smaller numbers of Weyl node pairs, Fermi energy closer to the nodes, and no other states near the Fermi energy. As described above, universality of the chiral anomaly related response in Weyl and Dirac metals is an emergent property, which becomes more precise as the energy is reduced toward the band-touching nodes. Currently, only Na_3Bi and $ZrTe_5$ come sufficiently close to the ideal limit of a topological semimetal to exhibit clear unequivocal transport signatures of the chiral anomaly, but this is certain to change in the near future as more topological semimetal materials are discovered.

DISCLOSURE STATEMENT

ACKNOWLEDGMENTS

LITERATURE CITED

1. Haldane FDM. 1988. *Phys. Rev. Lett.* 61:2015–18
2. Hasan MZ, Kane CL. 2010. *Rev. Mod. Phys.* 82:3045–67
3. Qi XL, Zhang SC. 2011. *Rev. Mod. Phys.* 83:1057–110
4. Volovik G. 2003. *The Universe in a Helium Droplet*. Oxford, UK: Clarendon
5. Haldane FDM. 2004. *Phys. Rev. Lett.* 93:206602
6. Volovik GE. 2007. In *Quantum Analogues: From Phase Transitions to Black Holes and Cosmology*, ed. W Unruh, R Schtzhold, vol. 718, *Lecture Notes in Physics*, pp. 31–73. Berlin/Heidelberg: Springer
7. Murakami S. 2007. *New J. Phys.* 9:356
8. Wan X, Turner AM, Vishwanath A, Savrasov SY. 2011. *Phys. Rev. B* 83:205101
9. Yang KY, Lu YM, Ran Y. 2011. *Phys. Rev. B* 84:075129
10. Burkov AA, Balents L. 2011. *Phys. Rev. Lett.* 107:127205
11. Burkov AA, Hook MD, Balents L. 2011. *Phys. Rev. B* 84:235126
12. Xu G, Weng H, Wang Z, Dai X, Fang Z. 2011. *Phys. Rev. Lett.* 107:186806
13. Young SM, Zaheer S, Teo JCY, Kane CL, Mele EJ, Rappe AM. 2012. *Phys. Rev. Lett.* 108:140405
14. Wang Z, Sun Y, Chen XQ, Franchini C, Xu G, et al. 2012. *Phys. Rev. B* 85:195320
15. Wang Z, Weng H, Wu Q, Dai X, Fang Z. 2013. *Phys. Rev. B* 88:125427
16. Xu SY, Belopolski I, Alidoust N, Neupane M, Bian G, et al. 2015. *Science* 349:613–17
17. Neupane M, Xu SY, Sankar R, Alidoust N, Bian G, et al. 2014. *Nat. Commun.* 5:3786
18. Lv BQ, Xu N, Weng HM, Ma JZ, Richard P, et al. 2015. *Nat. Phys.* 11:724–27
19. Lv BQ, Weng HM, Fu BB, Wang XP, Miao H, et al. 2015. *Phys. Rev. X* 5:031013
20. Lu L, Wang Z, Ye D, Ran L, Fu L, et al. 2015. *Science* 349:622–24
21. Yan B, Felser C. 2017. *Annu. Rev. Condens. Matter Phys.* 8:337–54
22. Hasan MZ, Xu SY, Belopolski I, Huang SM. 2017. *Annu. Rev. Condens. Matter Phys.* 8:289–309
23. Kohmoto M, Halperin BI, Wu YS. 1992. *Phys. Rev. B* 45:13488–93
24. Chang CZ, Zhang J, Feng X, Shen J, Zhang Z, et al. 2013. *Science* 340:167–70
25. Liu C-X, Zhang S-C, Qi X-L. 2016. *Annu. Rev. Condens. Matter Phys.* 7:301–21
26. Redlich AN. 1984. *Phys. Rev. Lett.* 52:18–21
27. Ludwig AWW, Fisher MPA, Shankar R, Grinstein G. 1994. *Phys. Rev. B* 50:7526–52
28. Fu L, Kane CL. 2007. *Phys. Rev. B* 76:045302
29. Halász GB, Balents L. 2012. *Phys. Rev. B* 85:035103
30. Adler SL. 1969. *Phys. Rev.* 177:2426–38
31. Bell JS, Jackiw R. 1969. *Nuovo Cim. A* 60:4
32. Alekseev AY, Cheianov VV, Fröhlich J. 1998. *Phys. Rev. Lett.* 81:3503–6
33. Zyuzin AA, Wu S, Burkov AA. 2012. *Phys. Rev. B* 85:165110
34. Vazifeh MM, Franz M. 2013. *Phys. Rev. Lett.* 111:027201
35. Zhang SC, Hu J. 2001. *Science* 294:823–28
36. Chen Y, Wu S, Burkov AA. 2013. *Phys. Rev. B* 88:125105
37. Burkov AA. 2014. *Phys. Rev. Lett.* 113:247203
38. Burkov AA. 2015. *Phys. Rev. B* 91:245157
39. Fukushima K, Kharzeev DE, Warringa HJ. 2008. *Phys. Rev. D* 78:074033
40. Son DT, Yamamoto N. 2012. *Phys. Rev. Lett.* 109:181602
41. Altland A, Bagrets D. 2016. *Phys. Rev. B* 93:075113

42. Son DT, Spivak BZ. 2013. *Phys. Rev. B* 88:104412

43. Lundgren R, Laurell P, Fiete GA. 2014. *Phys. Rev. B* 90:165115

44. Hirschberger M, Kushwaha S, Wang Z, Gibson Q, Liang S, et al. 2016. *Nat. Mater.* 15:1161–65

45. Spivak BZ, Andreev AV. 2016. *Phys. Rev. B* 93:085107

46. Lucas A, Davison RA, Sachdev S. 2016. *PNAS* 113:9463–68

47. Burkov AA, Kim YB. 2016. *Phys. Rev. Lett.* 117:136602

48. Xiong J, Kushwaha SK, Liang T, Krizan JW, Hirschberger M, et al. 2015. *Science* 350:413–16

49. Li Q, Kharzeev DE, Zhang C, Huang Y, Pletikosic I, et al. 2016. *Nat. Phys.* 12:550–54

50. Parameswaran SA, Grover T, Abanin DA, Pesin DA, Vishwanath A. 2014. *Phys. Rev. X* 4:031035

51. Abanin DA, Morozov SV, Ponomarenko LA, Gorbachev RV, Mayorov AS, et al. 2011. *Science* 332:328–30

52. Moll PJW, Nair NL, Helm T, Potter AC, Kimchi I, et al. 2016. *Nature* 535:266–70

53. Baum Y, Berg E, Parameswaran SA, Stern A. 2015. *Phys. Rev. X* 5:041046

54. Baireuther P, Hutasoit JA, Tworzyd J, Beenakker CWJ. 2016. *New J. Phys.* 18:045009

55. Jian-Hui Z, Hua J, Qian N, Jun-Ren S. 2013. *Chin. Phys. Lett.* 30:027101

56. Cortijo A, Ferreirós Y, Landsteiner K, Vozmediano MAH. 2015. *Phys. Rev. Lett.* 115:177202

57. Pikulin DI, Chen A, Franz M. 2016. *Phys. Rev. X* 6:041021

58. Grushin AG, Venderbos JWF, Vishwanath A, Ilan R. 2016. *Phys. Rev. X* 6:041046

59. Soluyanov AA, Gresch D, Wang Z, Wu Q, Troyer M, et al. 2015. *Nature* 527:495–98

60. Lee PA, Ramakrishnan TV. 1985. *Rev. Mod. Phys.* 57:287–337

61. Moll PJW, Potter AC, Nair NL, Ramshaw BJ, Modic KA, et al. 2016. *Nat. Commun.* 7:12492

62. Liu CX, Ye P, Qi XL. 2013. *Phys. Rev. B* 87:235306

63. Panfilov I, Burkov AA, Pesin DA. 2014. *Phys. Rev. B* 89:245103

64. Zhou J, Chang HR, Xiao D. 2015. *Phys. Rev. B* 91:035114

65. Araki Y, Nomura K. 2016. *Phys. Rev. B* 93:094438

66. Zhang XX, Nagaosa N. 2017. *Phys. Rev. B* 95:205143

67. Morimoto T, Nagaosa N. 2016. *Sci. Rep.* 6:19853

68. Meng T, Grushin AG, Shtengel K, Bardarson JH. 2017. *Phys. Rev. B* 94:155136

69. Meng T, Balents L. 2012. *Phys. Rev. B* 86:054504

70. Cho GY, Bardarson JH, Lu YM, Moore JE. 2012. *Phys. Rev. B* 86:214514

71. Wei H, Chao SP, Aji V. 2014. *Phys. Rev. B* 89:014506

72. Lu B, Yada K, Sato M, Tanaka Y. 2015. *Phys. Rev. Lett.* 114:096804

73. Bednik G, Zyuzin AA, Burkov AA. 2015. *Phys. Rev. B* 92:035153

74. Li Y, Haldane FDM. 2015. arXiv:1510.01730

75. Bednik G, Zyuzin AA, Burkov AA. 2016. *New J. Phys.* 18:085002